Objective Detection of Oceanic Eddies and the Agulhas Leakage

Francisco J. Beron-Vera, Yan Wang, and María J. Olascoaga

Rosenstiel School of Marine and Atmospheric Science, University of Miami, Miami, Florida

Gustavo J. Goni

National Oceanic and Atmospheric Administration/Atlantic Oceanographic and Meteorological Laboratory, Miami, Florida

George Haller

Institute for Mechanical Systems, ETH Zürich, Zurich, Switzerland

ABSTRACT

Mesoscale oceanic eddies are routinely detected from instantaneous velocities derived from satellite altimetry data. While simple to implement, this approach often gives spurious results and hides true material transport. Here it is shown how geodesic transport theory, a recently developed technique from nonlinear dynamical systems, uncovers eddies objectively. Applying this theory to altimetry-derived velocities in the South Atlantic reveals, for the first time, Agulhas rings that preserve their material coherence for several months, while ring candidates yielded by other approaches tend to disperse or leak within weeks. These findings suggest that available velocity-based estimates for the Agulhas leakage, as well as for its impact on ocean circulation and climate, need revision.

1. Introduction

Oceanic eddies are commonly envisaged as whirling bodies of water that preserve their shape, carrying mass, momentum, energy, thermodynamic properties, and biogeochemical tracers over long distances (e.g., Robinson 1983). While this widespread view on eddies is fundamentally Lagrangian (material), most available eddy detection methods are Eulerian (velocity based).

Eulerian detection of mesoscale eddies (with diameters ranging from 50 to 250 km) is routinely applied to instantaneous velocities derived from satellite altimetry measurements of sea surface height (SSH). In some cases, eddies are identified from the Okubo–Weiss criterion as regions where vorticity dominates over strain (e.g., Chelton et al. 2007; Henson and Thomas 2008; Isern-Fontanet et al. 2003; Morrow et al. 2004). In other cases, eddies are sought as regions filled with closed streamlines of the SSH field (e.g., Chelton et al. 2011a,b; Fang and Morrow 2003; Goni and Johns 2001) or as features obtained from a wavelet-packet decomposition of the SSH field (Doglioli et al. 2007; Turiel et al. 2007). These detection methods invariably use instantaneous Eulerian information to reach long-term conclusions about fluid transport. Furthermore, they give different results in reference frames that move or rotate relative to each other.

The problem with the use of instantaneous velocities is their inability to reveal long-range material transport and coherence in unsteady flows (Batchelor 1964). An example is shown in Fig. 1, where the instantaneous velocity field is classified as eddy-like for all times by each of the Eulerian criteria mentioned above. Specifically, vorticity dominates over strain, and streamlines are closed for all times. Yet actual particle motion turns out to be governed by a rotating saddle point with no closed transport barriers (Haller 2005).

Figure 1 also highlights the issue with frame-dependent eddy detection, whether Eulerian or Lagrangian. Truly unsteady flows have no distinguished reference frames: such flows remain unsteady in any frame (Lugt 1979). Conclusions about flow structures, therefore, should not depend on the chosen frame, because it is not a priori known which—if any—frame reveals those structures correctly.

Corresponding author address: F. J. Beron-Vera, RSMAS/AMP, University of Miami, 4600 Rickenbacker Cswy., Miami, FL 33149.
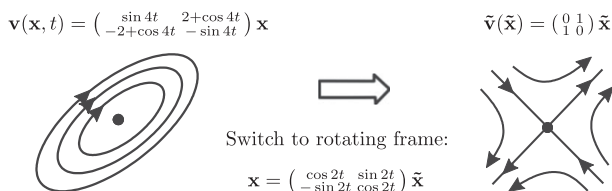E-mail: fberon@rsmas.miami.edu

$$\mathbf{v}(\mathbf{x}, t) = \begin{pmatrix} \sin 4t & 2 + \cos 4t \\ -2 + \cos 4t & -\sin 4t \end{pmatrix} \mathbf{x} \qquad\qquad \tilde{\mathbf{v}}(\tilde{\mathbf{x}}) = \begin{pmatrix} 0 & 1 \\ 1 & 0 \end{pmatrix} \tilde{\mathbf{x}}$$

Switch to rotating frame:

$$\mathbf{x} = \begin{pmatrix} \cos 2t & \sin 2t \\ -\sin 2t & \cos 2t \end{pmatrix} \tilde{\mathbf{x}}$$

FIG. 1. A planar unsteady velocity field identified as an eddy by Eulerian criteria. In an appropriate rotating frame, however, the velocity field becomes a steady saddle flow with no closed transport barriers.

Beyond conceptual problems, Eulerian eddy detection yields noisy results, necessitating the use of filtering and threshold parameters. Applying such detection methods to altimetry data, Souza et al. (2011) report variabilities up to 50% in the number of eddies detected, depending on the choice of parameters and filtering methods. A systematic comparison of these varying numbers with actual material transport is difficult because of the sparseness of in situ hydrographic measurements and Lagrangian data. In particular, most useful drifter trajectory data are only available from dedicated experiments, and satellite ocean color imagery is constrained by cloud cover or the absence of biological activity. This in turn implies that Eulerian predictions for Lagrangian eddy transport have remained largely unverified.

These shortcomings of contemporary eddy detection are important to consider when quantifying transport by eddies. For instance, recent studies suggest that long-range transport by anticyclonic mesoscale eddies (Agulhas rings) pinched off from the Agulhas Current retroflection is a potential moderating factor in global climate change. Known as the largest eddies in the ocean (Olson and Evans 1986), Agulhas rings transport warm and salty water from the Indian Ocean into the South Atlantic (Agulhas leakage). They may also possibly reach the upper arm of the Atlantic meridional overturning circulation (AMOC) when driven northwestward by the Benguela Current and its extension (Gordon 1986). Following an apparent southward shift in the subtropical front (Ridgway and Dunn 2007), the intensity of the Agulhas leakage has been on the rise (Biastoch et al. 2009), leading to speculation that it may counteract the slowdown of the AMOC because of Arctic ice melting in a warming climate (Beal et al. 2011). To assess this conjecture, an accurate Lagrangian identification of Agulhas rings is critical.

Indeed, most eddies identified from Eulerian footprints will disperse over relatively short times. While some of these dispersing features still drag water in their wakes, the transported water will stretch and fold because of the lack of a surrounding, coherent material boundary. As a consequence, distinguished features of the transported water, such as high temperature and salinity, will be quickly lost because of enhanced diffusion across filamented material boundaries.

Counteracting the effects of melting Arctic ice on AMOC requires a supply of warm and salty water (Beal et al. 2011). Agulhas rings with persistent and coherent material cores deliver this type of water directly from its source, the Agulhas leakage. By contrast, transient Eulerian ring-like features mostly stir the ocean without creating the clear northwest pathway for temperature and salinity envisioned by Gordon (1986).

In steady flow, coherent material eddies are readily identified as regions of closed streamlines. In near-steady flows with periodic time dependence, the Kolmogorov–Arnold–Moser (KAM) theory (cf., e.g., Arnold et al. 2006) reveals families of nested closed material curves (so-called KAM curves) that assume the same position in the flow after each temporal period. An outermost such KAM curve from a given family, therefore, plays the role of a coherent material eddy boundary. This result extends to near-steady time-quasiperiodic flows, in which KAM curves are quasiperiodically deforming closed material lines (Jorba and Simó 1996).

Identifying similar material boundaries for coherent eddies in general unsteady flows has been an open problem. Recently, however, Haller and Beron-Vera (2012) developed a new mathematical theory of transport barriers that, among other features, identifies generalized KAM curves (elliptic transport barriers) for arbitrary unsteady flows. Here we use this new theory to devise a methodology, geodesic eddy detection, for the objective identification of Lagrangian eddy boundaries in the ocean.

Analyzing altimetry measurements in the eastern side of the South Atlantic subtropical gyre, we find that geodesic eddy detection significantly outperforms available Eulerian and Lagrangian methods in locating long-lived and coherent Agulhas rings. An independent analysis of available satellite ocean color (chlorophyll) data corroborates our results by showing localized and persistent biological activity in an eddy identified using geodesic eddy detection. Our findings suggest that Eulerian estimates of the volume of water transported by Agulhas rings in a coherent manner are significantly exaggerated.

Geodesic eddy detection is outlined in section 2, which is organized into four subsections. Section 2a presents the dynamical systems setup for studying material transport. The rationale behind the geodesic transport theory of Haller and Beron-Vera (2012) is reviewed in section 2b. Section 2c covers the notion of shear transport barriers. The definition of coherent material eddy boundary is given in section 2d. Our main results are presented in section 3. The conclusions are stated in section 4. Appendix A describes the velocity data on which geodesic
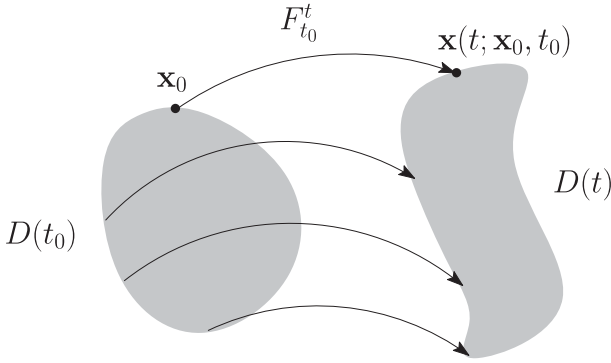
FIG. 2. A fluid domain at time t_0, $D(t_0)$, deformed under the flow map, $F_{t_0}^t : \mathbf{x}_0 \mapsto \mathbf{x}(t; \mathbf{x}_0, t_0)$, into a domain $D(t)$ at time $t \neq t_0$ along fluid particle trajectories.

FIG. 3. Minimal stretching property of a material curve γ_{t_0}, for times t sufficiently larger than t_0, in a steady circular shear flow among material curves with the same endpoints, $\hat{\gamma}_{t_0}$ and $\bar{\gamma}_{t_0}$. Note that $\hat{\gamma}_{t_0}$ and $\bar{\gamma}_{t_0}$ stretch longer than γ_t, regardless of whether they are initially shorter or longer than γ_{t_0}.

eddy detection is applied. The algorithmic steps of geodesic eddy detection are summarized in appendix B. Finally, computational details are given in appendix C.

2. Geodesic eddy detection

a. Dynamical systems setup

Consider an unsteady flow on the plane with velocity field $\mathbf{v}(\mathbf{x}, t)$, where $\mathbf{x} = (x, y)$ denotes position and t is time. The evolution of fluid particle positions in this flow satisfies a nonautonomous dynamical system given by the following differential equation:

$$\frac{d\mathbf{x}}{dt} = \mathbf{v}(\mathbf{x}, t). \tag{1}$$

Material transport in (1) is determined by the properties of the flow map,

$$F_{t_0}^t : \mathbf{x}_0 \mapsto \mathbf{x}(t; \mathbf{x}_0, t_0), \tag{2}$$

which takes an initial fluid particle position $\mathbf{x}_0$ at time t_0 to its later position $(t; t_0, \mathbf{x}_0)$ at time $t \neq t_0$, along trajectories of (1) (Fig. 2).

When obtained from satellite altimetry (cf. appendix A), the velocity field in (1) is a temporally aperiodic, highly unsteady finite-time dataset. Material transport in the resulting flow, therefore, cannot be described by classic dynamical systems methods, such as those surveyed by Ottino (1989). Instead, we adopt the recent approach of Haller and Beron-Vera (2012) by seeking transport barriers in (1) near least-stretching material lines.

b. Transport barriers as geodesics

As noted in Haller and Beron-Vera (2012), the least-stretching behavior of transport barriers is observed in several canonical flow examples where they are known to
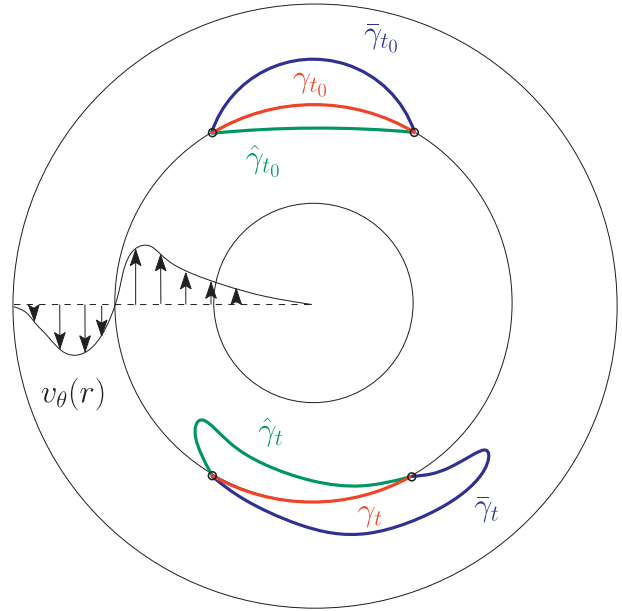
exist. Examples include steady flow around a stagnation point, steady shear jet flow, and steady circular shear flow.

Of particular relevance for our purposes here is the steady circular shear flow, the prototype of a coherent eddy. The least-stretching property of circular transport barriers in this flow is illustrated in Fig. 3. Indeed, for sufficiently long time, perturbations to a reference material curve lying on a closed streamline grow longer than the reference curve, even if the perturbation was initially shorter than this curve.

Similar behavior is seen for KAM curves in near-steady time-periodic and quasiperiodic flows. As noted earlier, nested families of KAM curves in such flows objectively indicate the presence of coherent material eddies. The stretching of material lines off a KAM curve is due to the twist (shear) across the curve, which may be even magnified by the presence of resonance islands.

In a time-aperiodic flow defined over a finite-time interval, locating at time t_0 the positions of material lines that will stretch the least over the time interval (t_0, t) leads to a variational problem. As shown in Haller and Beron-Vera (2012), the solutions of this problem are distinguished material curves at time t_0 that turn out to be minimal geodesics (shortest paths) of the metric generated by the Cauchy–Green strain tensor,

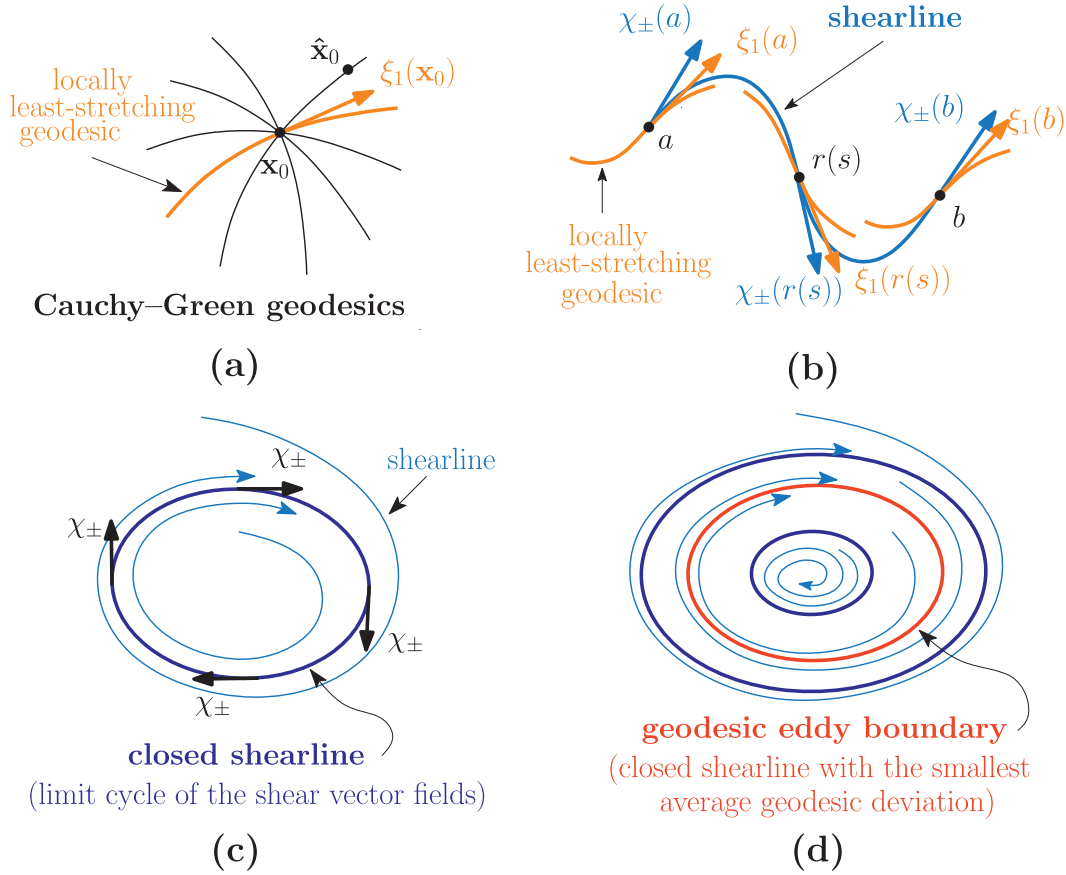$$C_{t_0}^t(\mathbf{x}_0) = \nabla F_{t_0}^t(\mathbf{x}_0)^{\mathrm{T}} \nabla F_{t_0}^t(\mathbf{x}_0), \tag{3}$$

FIG. 4. (a) Cauchy–Green geodesics emanating from an initial position $\mathbf{x}_0$, representing least-stretching curves out of all material curves connecting two initial positions, such as $\mathbf{x}_0$ and $\hat{\mathbf{x}}_0$. The locally least-stretching geodesic at $\mathbf{x}_0$ is tangent to the weakest strain eigenvector ξ_1 of the Cauchy–Green tensor, a quantity commonly used to measure deformation in continuum mechanics. (b) Shearlines are curves tangent to the Lagrangian shear vector fields $\chi_\pm$, along which an objective (i.e., frame independent) measure of shear is maximized. A shear barrier at time t_0 between points a and b is a shearline shadowed by locally least-stretching geodesics. (c) Closed shearlines are limit cycles of the $\chi_\pm$ vector fields. (d) A geodesic eddy boundary is a member of a nested limit cycle family with the smallest average geodesic deviation. (The family may also just consist of one member.)

where superscript T denotes transpose and ∇ refers to the spatial gradient operator.

From each point $\mathbf{x}_0$ in the initial flow configuration, Cauchy–Green geodesics emanate in all possible directions. In fact, any pair of points on the plane are connected by a unique Cauchy–Green geodesic, which is locally the least-stretching material line out of all material lines connecting those two points (Fig. 4a).

Among all geodesics passing through $\mathbf{x}_0$, the locally least-stretching geodesic at $\mathbf{x}_0$ is of particular interest. This geodesic is tangent to the direction of minimal strain at $\mathbf{x}_0$. More specifically, consider

$$C_{t_0}^t \xi_i(\mathbf{x}_0) = \lambda_i(\mathbf{x}_0)\xi_i(\mathbf{x}_0), \quad 0 < \lambda_1(\mathbf{x}_0) \leq \lambda_2(\mathbf{x}_0), \quad \text{and}$$

$$|\xi_i(\mathbf{x}_0)| = 1, \quad i = 1, 2,$$

(4)

where $\lambda_i(\mathbf{x}_0)$ and $\xi_i(\mathbf{x}_0)$ are the ith eigenvalue and eigenvector of $C_{t_0}^t(\mathbf{x}_0)$, respectively, and $|\cdot|$ denotes Euclidean norm. Then the locally least-stretching geodesic through $\mathbf{x}_0$ is tangent to the weakest strain eigenvector at $\mathbf{x}_0$, $\xi_1(\mathbf{x}_0)$, as shown in Fig. 4a.

Typical geodesics in a turbulent flow still stretch by a relatively large amount, even though they stretch less than any other curve connecting their endpoints. Most geodesics, therefore, do not act as observable transport barriers. Observable barriers, however, must necessarily run close to locally least-stretching geodesics. This means that at each point $\mathbf{x}_0$ of an observable transport barrier, both the tangent and the curvature of the barrier must be close to the tangent and curvature of the locally least-stretching geodesic through $\mathbf{x}_0$. For short, we say that such a barrier is a material line that is geodesically shadowed over the time interval (t_0, t).

c. Shear barriers

With the behavior of streamlines in the steady circular flow example in mind, it is natural to seek the transport barriers of interest as those maximizing shear. An appropriate frame-independent form of shear in unsteady flows is given by the Lagrangian shear, defined as the tangential projection of the linearly advected normal to a material line. As shown in Haller and Beron-Vera (2012), Lagrangian-shear-maximizing transport barriers (or shear barriers) over (t_0, t) turn out to be geodesically shadowed trajectories of the Lagrangian shear vector fields

$$\chi_{\pm}(\mathbf{x}_0) = \alpha_1(\mathbf{x}_0)\xi_1(\mathbf{x}_0) \pm \alpha_2(\mathbf{x}_0)\xi_2(\mathbf{x}_0),$$

$$\alpha_i(\mathbf{x}_0) = \sqrt{\frac{\sqrt{\lambda_j(\mathbf{x}_0)}}{\sqrt{\lambda_1(\mathbf{x}_0)} + \sqrt{\lambda_2(\mathbf{x}_0)}}}, \quad i \neq j. \quad (5)$$

Closeness of a trajectory (or shearline) of (5) to its shadowing least-stretching geodesic at $\mathbf{x}_0$ can be computed as the sum of their tangent and curvature differences. This sum, the geodesic deviation of a shearline, can be proven to be equal to (Haller and Beron-Vera 2012)

$$d_g^{\chi_{\pm}}(\mathbf{x}_0) = |1 - \alpha_1| + \left| \left(\alpha_1 + \frac{\lambda_1}{\lambda_2} - 1\right)\kappa_1 \mp \alpha_2\kappa_2 \right.$$
$$\left. \mp \frac{\boldsymbol{\nabla}\alpha_1 \cdot \chi_{\pm}}{\alpha_2} - \frac{\boldsymbol{\nabla}\lambda_1 \cdot \xi_2}{2\lambda_2} \right|, \quad (6)$$

where

$$\kappa_i(\mathbf{x}_0) = \boldsymbol{\nabla}\xi_i(\mathbf{x}_0)\xi_i(\mathbf{x}_0) \cdot \xi_j(\mathbf{x}_0), \quad i \neq j \quad (7)$$

is the curvature of the curve tangent to the ith strain eigenvector field at $\mathbf{x}_0$ (Fig. 4b).

Shear barriers are either open curves (parabolic barriers) or closed curves (elliptic barriers). While sets of parabolic barriers generalize the concept of a shear jet to arbitrary unsteady flow, elliptic barriers generalize the concept of a KAM curve. As limit cycles of the shear vector field (Fig. 4c), elliptic barriers are robust with respect to perturbations of the underlying velocity data, and hence smoothly persist under moderate noise and small changes to the observational time interval (t_0, t).

d. Eddy boundaries

If elliptic barriers occur in a nested family, the outermost barrier is the physically observed eddy boundary, enclosing the largest possible coherent water mass in the region. Outermost elliptic barriers, however, also tend
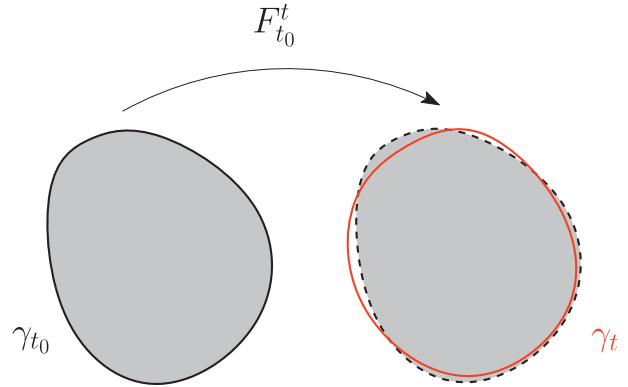

FIG. 5. Schematics of a closed shearline γ_{t_0} computed using flow data over the time interval (t_0, t). The dashed curve indicates a translated and rotated position of γ_{t_0} for reference. If the flow is incompressible, the advected material line γ_t has the same arclength, and encloses the same area, as γ_{t_0}.

to be the most sensitive to errors and uncertainties in the velocity data.

To obtain a robust eddy boundary, we select the member of a nested family of closed shearlines which has the lowest average geodesic deviation, $\langle d_g^{\chi_{\pm}} \rangle$, in the family (Fig. 4d). As discussed in Haller and Beron-Vera (2012), $\langle d_g^{\chi_{\pm}} \rangle$ along an elliptic barrier measures how much the barrier extraction procedure has converged over the time interval (t_0, t). Accordingly, an elliptic barrier with the lowest $\langle d_g^{\chi_{\pm}} \rangle$ value in a nested family of barriers is the best eddy barrier candidate. As such, it is also the least susceptible to errors and uncertainties. Based on these considerations, geodesic eddy detection comprises the algorithmic steps described in appendix B.

We finally note that, in incompressible flows, elliptic barriers have two important conservation properties: 1) they preserve the area they enclose and 2) they reassume their initial arclength at time t (Fig. 5) (Haller and Beron-Vera 2012). These two properties make elliptic barriers ideal boundaries for coherent eddy cores.

3. Results

We consider a region of the South Atlantic subtropical gyre, bounded by longitudes (14°W, 9°E) and latitudes (39°S, 21°S), which encompasses possible routes of Agulhas rings (dashed rectangle in each panel of Figs. 7 and 9). The same region has been analyzed by Beron-Vera et al. (2008), who showed that the finite-time Lyapunov exponent, a widely used Lagrangian diagnostic (Haller 2001; Peacock and Dabiri 2010), does not reveal coherent material eddies. More recently, the same area was also studied by Lehahn et al. (2011), who reported observations of a nearly isolated mesoscale chlorophyll patch,

traversing the region in the period from November 2006 to September 2007.

We apply geodesic eddy detection to altimetry-derived currents (cf. appendix A) in the selected region starting on $t_0 = 24$ November 2006, with the detection time scale set to $T = t - t_0 = 90$ days. Following the algorithmic steps described in appendix B, with numerical details given in appendix C, geodesic eddy detection isolates two coherent material eddies (denoted geodesic eddies). The boundary of the first eddy is obtained as a limit cycle of the $\chi^+(\mathbf{x}_0)$ shear vector field, with an anticyclonic polarity. The boundary of the second eddy is recovered as a limit cycle of the $\chi^-(\mathbf{x}_0)$ field, with a cyclonic polarity. The extraction of the anticyclonic eddy boundary is detailed in Fig. 6. The geographical locations of the two eddies identified on 24 November 2006 are shown in the upper-left panel of Fig. 7, with the anticyclonic eddy indicated in red and the cyclonic eddy in blue.

The remaining panels in the left column of Fig. 7 show several later advected positions of the two geodesic eddies to illustrate their coherence. Note the complete lack of material filamentation or leakage from these eddies over 90 days. This can be seen in more detail in the right column of Fig. 8, which shows the two eddies on the detection date and 90 days later. Closed material lines like the boundaries of these eddies are highly atypical in an otherwise turbulent flow. Their role is indeed best compared to the role of KAM curves in time-periodic or quasiperiodic flows.

Remarkably, the coherence of the anticyclonic eddy is preserved well over the 90-day period on which our computations were performed (Fig. 9, left column). Indeed, this eddy preserves its coherence even 540 days later, exhibiting only translation, rotation, and minor deformation without noticeable leakage, stretching or folding. The remarkable coherence of this eddy can attributed to its interior being foliated by a large number of nested closed shearlines. The inner shearlines are less exposed to the ambient turbulent mixing than the outer ones, thereby providing a stability buffer for the eddy. By contrast, the boundary of the cyclonic eddy is the only member of a family of nested closed shearlines. With the stability buffer absent, the boundary of this eddy exhibits filamentation immediately after 90 days.

For comparison, the remaining columns of Fig. 7 illustrate the accuracy of the two most widely used Eulerian eddy diagnostics and one recent Lagrangian eddy diagnostic on the same dataset.

The middle-left column of Fig. 7 shows the material evolution of eddies (denoted SSH eddies) obtained from the method of Chelton et al. (2011b), who argue that closed SSH contours can play roughly the same role in inhibiting transport as closed streamlines do in steady
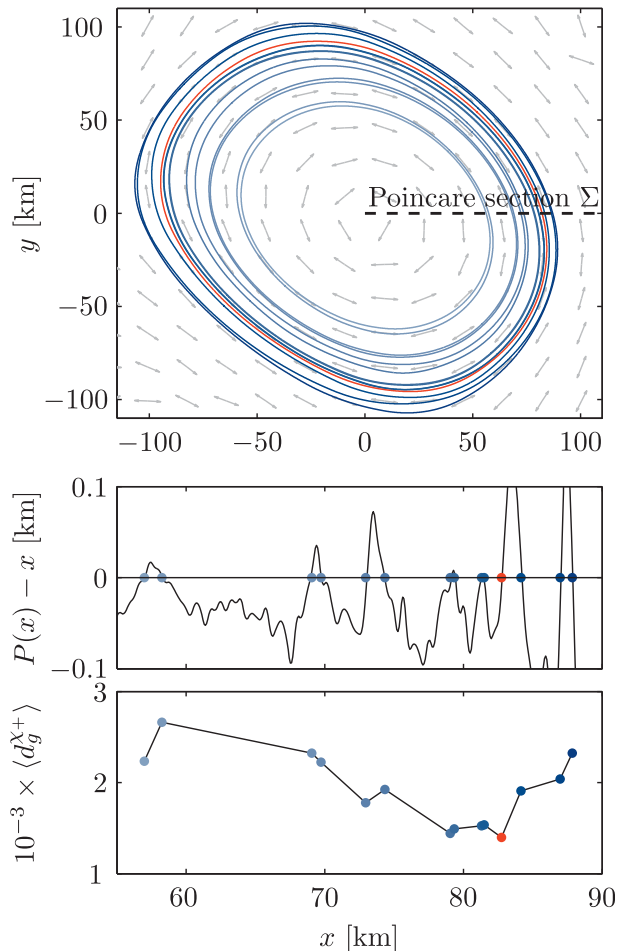

FIG. 6. Identification of a coherent material eddy boundary on $t_0 = 24$ November 2006 from geodesic eddy detection with detection time scale $T = t - t_0 = 90$ days. Marked in red, the eddy boundary is obtained as an average-geodesic-deviation-minimizing member of a nested family of limit cycles of the Lagrangian shear vector field χ_+. (top) The full limit cycle family is shown in blue, with gray arrows indicating the χ_+ vector field. (middle) The first return (Poincaré) map, $x \mapsto P(x)$, onto a section Σ locally transverse to χ_+ vector field is shown. Dots indicate the fixed points of the Poincaré map, $P(x) = x$, corresponding to each of the limit cycles. (bottom) The distribution of the average geodesic deviation over the limit cycles is shown.

flows. Chelton et al. (2011b) suggest that this should be the case when the rotational speed of the eddy U dominates its translational speed, c (cf. also Early et al. 2011). More specifically, Chelton et al. (2011b) propose that $U/c > 1$ should signal the presence of a coherent eddy, as opposed to a linear wave ($U/c < 1$). However, as revealed by the Lagrangian evolution of closed SSH contours in the upper-middle row of Fig. 7 (all with $U/c > 1$ over at least 90 days), most such contours rapidly stretch and fold, exhibiting leakage and filamentation that disqualifies them as physically reasonable coherent
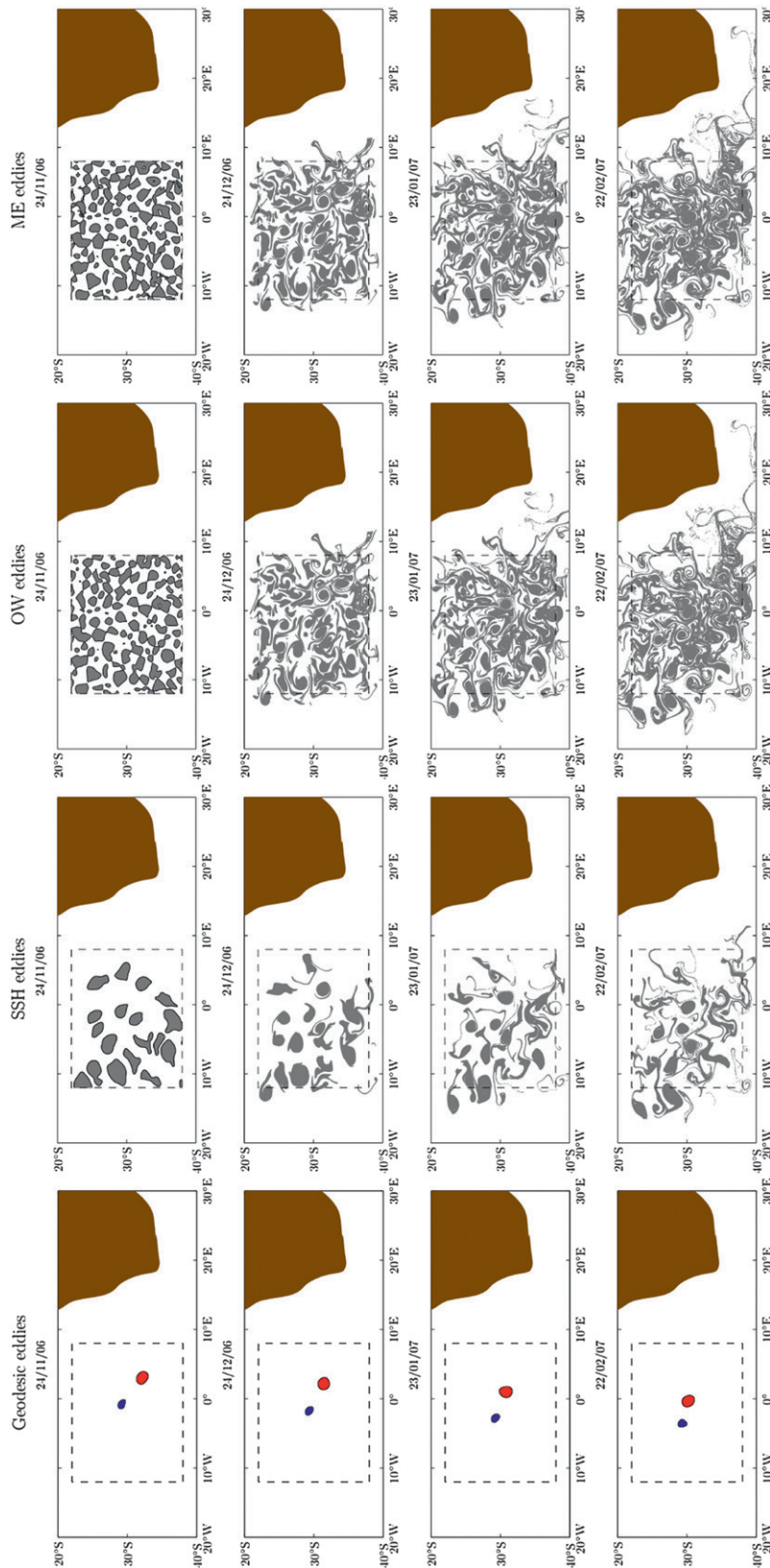
FIG. 7. (left) Selected snapshots of the 90-day evolution of fluid inside eddies identified by geodesic eddy detection; (middle left) the method of Chelton et al. (2011a) with $U/c > 1$ over at least 90 days; (middle right) the Okubo–Weiss (OW) criterion; and (right) the criterion of Mézic et al. (2010).
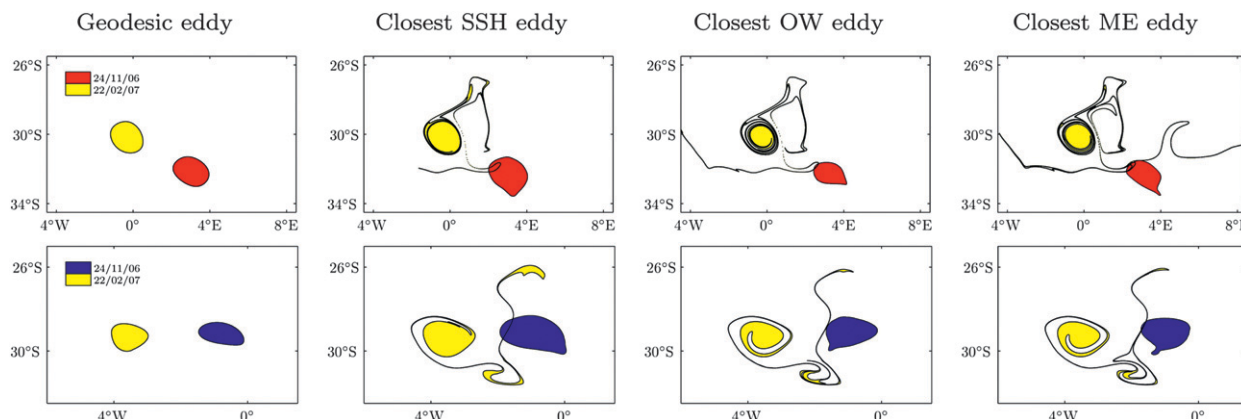
FIG. 8. Fluid positions of eddy candidates obtained from different detection methods on $t_0 = 24$ Nov 2006 and 90 days later. (middle left, middle right, and right columns) The red and blue eddy candidates by other eddy detection methods are the closest ones to (left) the similarly colored geodesic eddies.

material eddy boundaries. Only two SSH eddies approximate coherent geodesic eddies on 24 November 2006 (Fig. 8, middle-left column). However, both eddies exhibit almost instantaneous material filamentation beyond that date. The panels in the right column of Fig. 9 further demonstrate the inability of an SSH eddy with $U/c > 1$ for a period of at least 540 days to trap and carry within water in a coherent manner. We conclude that the SSH contour approach, with or without the $U/c > 1$ requirement, shows major inaccuracies in detecting material eddies, including the overestimation of coherent material eddy cores, as well as the generation of a large number of false positives.[1]

The middle-right column of Fig. 7 documents similar findings for the Okubo–Weiss criterion (Okubo 1970; Weiss 1991), the other broadly used frame-dependent Eulerian method for eddy identification. Relative to a reference frame, this method identifies eddies (denoted OW eddies) as regions of fluid where vorticity dominates over strain. The regions indicated in black qualify as OW eddies in the earth's frame on 24 November 2006. In a similar manner to SSH eddies, coherent geodesic eddies on 24 November 2006 are roughly approximated by two OW eddies, which deform rapidly after that date (Fig. 8, middle-right column). The remaining OW eddies are false positives for Lagrangian eddies: they undergo intense stretching and filamentation, before fully dispersing a few months later. We conclude that when used for coherent material eddy detection, the Okubo–Weiss approach also shows major inaccuracies. This includes the inability to capture actual coherent eddies accurately, as well as well as the tendency to generate numerous false

positives. False negatives also arise once threshold values (not discussed) are introduced for the Okubo–Weiss parameter.

We now proceed to consider the application of the more recent Lagrangian eddy diagnostic of Mézic et al. (2010). This approach views an incompressible flow region at time t_0 as a mesoelliptic region if the eigenvalues of the deformation gradient $\nabla F_{t_0}^t(\mathbf{x}_0)$ are complex for all $\mathbf{x}_0$ in that region. Even though this approach is Lagrangian, the eigenvalues of $\nabla F_{t_0}^t(\mathbf{x}_0)$ are frame dependent, and hence the resulting eddy candidates are not objective. As noted in Mézic et al. (2010), mesoelliptic regions approach Okubo–Weiss elliptic regions as t tends to t_0. For increasing $T = t - t_0$, mesoelliptic regions (denoted ME eddies) tend to rapidly fill the full domain of extraction, as most initial conditions accumulate enough rotation in their evolution to create complex eigenvalues for $\nabla F_{t_0}^t(\mathbf{x}_0)$. As a result, identifying ME eddies over time scales longer than a few days becomes unrealistic. Instead, we have chosen to use $T = 4$ days, following Mézic et al. (2010).

Shown in the right colum of Fig. 7, ME eddies resemble OW eddies closely, as expected. In a fashion similar to OW eddies, only two ME eddies approximate the geodesic eddies detected on 24 November 2006. Just as OW eddies, these ME eddies develop substantial material filamentation beyond that date (Fig. 8, right column).

Independent observational evidence for the Lagrangian eddies can be inferred from surface ocean chlorophyll concentration in the South Atlantic. Figure 10 shows a sequence of snapshots of chlorophyll concentration derived from the Moderate Resolution Imaging Spectroradiometer (MODIS) sensor aboard the *Aqua* satellite. Note the patch of high chlorophyll concentration, discussed in Lehahn et al. (2011), which translates inside

---

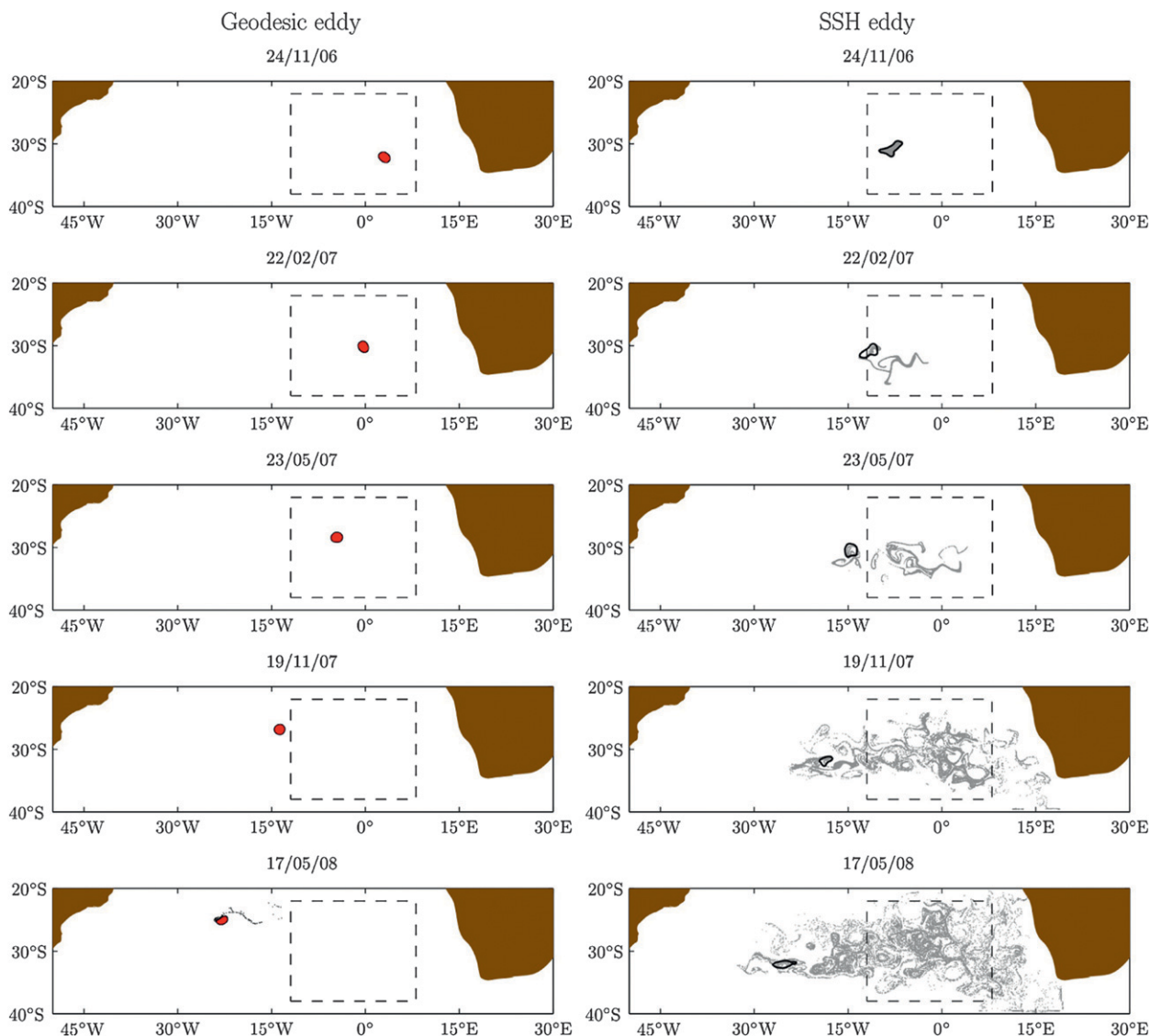[1] Indeed, $U/c \to \infty$ in the flow defined in Fig. 1.

FIG. 9. Selected snapshots of the 540-day evolution of fluid inside (left) a geodesic eddy and (right) an SSH eddy. The instantaneous SSH contour that defines the SSH eddy, which has $U/c > 1$ over at least 540 days, is indicated.

the anticyclonic geodesic eddy detected on 24 November 2006 from this date through 23 May 2007. Because of the lack of filamentation in the ring boundary, the diffusion of chlorophyll is moderate and remains confined to the periphery of the ring. This observation confirms the ability of Lagrangian eddies to preserve the concentration peaks of diffusive substances over long distances.

We now derive estimates for the volume of water carried by eddies obtained from different methods. For simplicity, we assume that the eddies are quasigeostrophic and equivalent barotropic, with their base lying on the 10°C isotherm at a depth of 400 m (Garzoli et al. 1999). Under these assumptions, we obtain the volume estimates in Table 1 for a single day, with other dates

giving similar results. The volume estimates are grouped by the polarity of the eddies involved, with anticyclonic eddies being candidates for Agulhas rings.

OW eddies have been reported to overestimate eddy transport rates based on comparisons with other Eulerian estimates (Souza et al. 2011), as opposed to comparisons with observed material transport. The volume estimates in Table 1 show that even other Eulerian indicators, such as closed streamlines of the SSH field with $U/c > 1$ as proposed by Chelton et al. (2011b), significantly overestimate the volume of coherent material eddies. The same observation applies to the Lagrangian indicator introduced by Mézic et al. (2010). A recent set-theoretical study (Froyland et al. 2012) of a three-dimensional
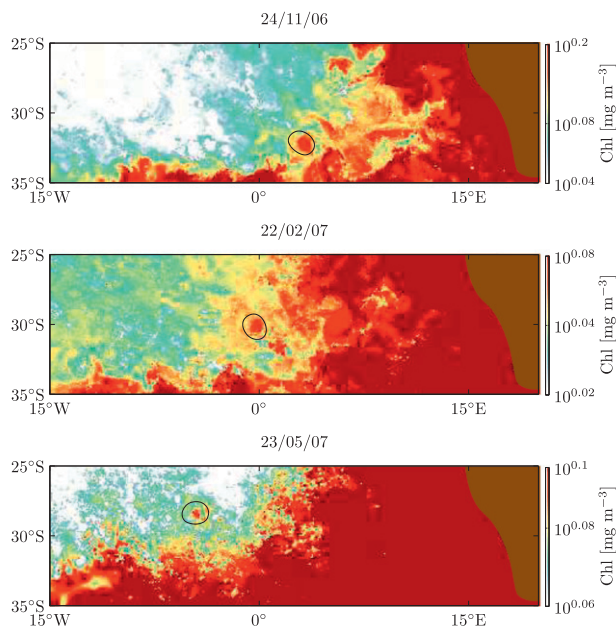
FIG. 10. Sequence of snapshots of satellite-derived surface ocean chlorophyll concentration with the boundary of the anticyclonic geodesic eddy detected on 24 Nov 2006 overlaid. The color scale varies from figure to figure to aid the visualization of chlorophyll anomalies.

Agulhas ring produced by an ocean general circulation model also yields results similar to those from the Eulerian techniques surveyed here. This provides further illustration that Lagrangian approaches also lead to exaggerated transport estimates, if they fail to capture the frame-independent details of material stretching.

Note that the coherently transported water mass (Table 1, left column) is carried mostly by an anticyclonic geodesic eddy. As an impermeable whirling body of water showing minor deformation over roughly a year-and-a-half period, such an eddy represents an exact mathematical construction of what has been (somewhat loosely) defined as a mesoscale ring in oceanography. Furthermore, this particular ring is best referred to as an Agulhas ring, as its backward-time advection (not shown) to the Agulhas retroflection area confirms. Thus, by Table 1, actual transport of warm and salty water by (coherent material) Agulhas rings is about one order of magnitude less than what can be deduced from available nonobjective eddy detection methods.

To illustrate the general validity of these conclusions, we present in Table 2 the results from a more extended survey of the volume carried by geodesic and SSH eddies in the years 1997, 2002, and 2007. In agreement with the results discussed above, the volume of eddies identified in the Eulerian frame is found to be always significantly larger than that of geodesic eddies, thereby

TABLE 1. Estimated volume (10^4 km^3) of water warmer than 10°C carried by eddies on 24 Nov 2006, grouped by their polarity, as identified by different eddy detection methods.

	Geodesic eddies	SSH eddies	OW eddies	ME eddies
Cyclonic	0.5	11.5	19.2	19.8
Anticyclonic	1.0	23.5	35.4	37.2

overestimating the volume of water that can be transported coherently. Consistent with numerical simulations (Biastoch et al. 2009), which suggest that the Agulhas leakage has been increasing, the volume of geodesic eddies (of both polarities) follows a similar trend. Clearly, to confirm this trend and correctly assess the role of geodesic eddies in the Agulhas leakage, a detailed survey is needed. Such a survey will require an automated geodesic eddy detection scheme, whose construction is currently underway.

We reiterate that coherent material transport (as opposed to the widespread dispersion of SSH, OW, and ME eddies observed in Fig. 7) is the relevant metric for quantifying the transport of diffusive quantities, such as salinity and temperature. Indeed, the disintegration of SSH, OW, and ME eddy candidates is accompanied by the erosion of salinity and temperature differences between the water they carry in their wake and the water they traverse.

The use of filters, thresholds, and size-limits would undoubtedly reduce the eddy count and transport estimates obtained from nonobjective detection methods. Such postprocessing steps, however, are largely heuristic: they exploit the high sensitivity of the underlying nonobjective detection methods to bring them in line with each other, and with sporadic in situ hydrographic measurements (Souza et al. 2011). We stress that geodesic eddy detection has no such tuning parameters, and the underlying mathematics (structural stability of limit cycles) renders its conclusions robust.

4. Conclusions

We have introduced a new method, geodesic eddy detection, for the objective (frame independent) identification and tracking of mesoscale eddies in the ocean. In short, geodesic eddy boundaries are limit cycles of the

TABLE 2. Estimated volume (10^4 km^3) of water warmer than 10°C carried by eddies along the years. Indicated in parentheses is the volume estimate corresponding to eddies with anticyclonic polarity.

	Year 1997	Year 2002	Year 2007
Geodesic eddies	7 (5)	10 (9)	9 (7)
SSH eddies	63 (29)	62 (36)	57 (27)

Lagrangian shear vector field that are the closest to least-stretching geodesics of the Cauchy–Green strain tensor. When tracked as material lines, geodesic eddy boundaries in a two-dimensional incompressible flow preserve their enclosed area and arclength, acting as impenetrable islands of minimal deformation in an otherwise turbulent flow. This in turn enables them to preserve the concentration of diffusive tracers they carry for extended periods. By the structural stability of limit cycles, geodesic eddy boundaries are robust with respect velocity measurement errors and changes in their detection period.

Using geodesic eddy detection, we have isolated highly coherent Agulhas rings that carry warm and salty water over large distances. Remarkably, one geodesic eddy constructed from three months of data was found to show no sign of disintegration up to one year and a half. By comparison, eddies identified by two currently used Eulerian methods and one recent Lagrangian diagnostic showed clear signs of leakage and stretching within weeks. The volume of water that such eddies would transport if they were coherent was found to be about an order of magnitude larger than the volume of water transported by actual coherent material eddies. Satellite observations of a highly coherent chlorophyll patch provided independent confirmation that geodesically detected Agulhas rings carry diffusive substances over large distances.

We argue that geodesically detected Agulhas rings are better positioned to impact AMOC than their counterparts obtained from nonobjective methods. Indeed, the latter rings lack a coherent material boundary and hence the ability to deliver warm and salty water effectively into the upper arm of AMOC. Our argument does assume that the geodesically detected Agulhas rings are not trapped within the subtropical gyre. A verification of this assumption is currently underway.

The present analysis is based on forward-time integration of the surface velocity field and hence is appropriate for a historical assessment of eddy formation and transport. In a real-time operational setting, geodesic eddy boundaries are determined from backward integration, that is, from reverse fluid motion available up to the present time. Undoubtedly, both the forward-time and the backward-time Lagrangian analyses are computationally more demanding than an assessment of the SSH field, either instantaneous or over time. By nature, however, Lagrangian calculations are highly parallelizable, benefiting from up to two orders of magnitude speed ups on multiprocessor clusters (Conti et al. 2012; Garth et al. 2007).

In our view, an investment in additional computational resources is well justified by the objectivity of the results, which promises a better assessment of the role of transport by mesoscale eddies in global ocean circulation and climate.

APPENDIX A

Velocity Data

Eulerian eddy detection is routinely applied to satellite altimetry measurements, a unique source of SSH data for global monitoring of mesoscale variability available continually since the early 1990s (Fu et al. 2010). The basis for this is the assumption of a geostrophic balance in which the pressure gradient is caused by differences in SSH, with the resulting currents reflecting an integral dynamic effect of the density field above the thermocline.

The velocity field $\mathbf{v}(\mathbf{x}, t)$ in (1) is thus assumed to be of the form

$$\mathbf{v}(\mathbf{x}, t) = \left[-\frac{g}{f} \frac{\partial \eta(\mathbf{x}, t)}{\partial y}, \frac{g}{f} \frac{\partial \eta(\mathbf{x}, t)}{\partial x} \right]. \quad \text{(A1)}$$

Here $\mathbf{x} = (x, y)$ denotes position on a plane with Cartesian x (y) zonal (meridional) coordinate; $\eta(\mathbf{x}, t)$ denotes SSH; f is the Coriolis parameter (twice the local vertical component of the earth's angular velocity); and g is the acceleration of gravity. While we choose to work on a planar domain here for simplicity, the underlying geodesic transport theory also applies to flows on a sphere (Haller and Beron-Vera 2012).

The background η component is steady, given by a mean dynamic topography constructed from altimetry data, in situ measurements, and a geoid model (Rio and Hernandez 2004). The perturbation η component is transient, given by altimetric SSH anomaly measurements provided weekly on a 0.25°-resolution longitude–latitude grid. This perturbation component is referenced to a 7-yr (1993–99) mean, obtained from the combined processing of a constellation of available altimeters (Le Traon et al. 1998).

APPENDIX B

Algorithmic Steps of Geodesic Eddy Detection

Geodesic eddy detection for the flow defined by (1) and (A1) involves the following computational steps.

1) Fix a grid $\mathcal{G}_0$ of initial positions in the flow domain of interest, and time scale T over which coherent eddies are to be tracked. For each initial condition $\mathbf{x}_0 \in \mathcal{G}_0$, integrate the nonautonomous dynamical system (1) from an initial time t_0 to time $t = t_0 + T$. This leads to a discrete approximation of the flow map $F_{t_0}^t$ defined in (2) over the grid $\mathcal{G}_0$.

2) Compute the deformation gradient field $\mathbf{V}F_{t_0}^t(\mathbf{x}_0)$. Using central differences over a rectangular $\mathcal{G}_0$ this can be achieved as follows. Let $\mathbf{x}_t^{i,j} = (x_t^{i,j}, y_t^{i,j})$ denote the image under the flow map $F_{t_0}^t$ of a point $\mathbf{x}_0^{i,j} = (x_0^{i,j}, y_0^{i,j}) \in \mathcal{G}_0$. Then

$$\mathbf{V}F_{t_0}^t(\mathbf{x}_0^{i,j}) = \begin{pmatrix} \dfrac{x_t^{i+1,j} - x_t^{i-1,j}}{x_0^{i+1,j} - x_0^{i-1,j}} & \dfrac{x_t^{i,j+1} - x_t^{i,j-1}}{y_0^{i,j+1} - y_0^{i,j-1}} \\[3mm] \dfrac{y_t^{i+1,j} - y_t^{i-1,j}}{x_0^{i+1,j} - x_0^{i-1,j}} & \dfrac{y_t^{i,j+1} - y_t^{i,j-1}}{y_0^{i,j+1} - y_0^{i,j-1}} \end{pmatrix}. \quad \text{(B1)}$$

3) Construct the Cauchy–Green strain tensor field $C_{t_0}^t(\mathbf{x}_0)$ defined in (3), and compute its eigenvalue and eigenvector fields, $\lambda_i(\mathbf{x}_0)$ and $\xi_i(\mathbf{x}_0)$, as defined in (4). The following are explicit formulas:

$$\lambda_1 = \frac{1}{2}\mathcal{T} - \sqrt{\frac{1}{4}\mathcal{T}^2 - \mathcal{D}}, \quad \lambda_2 = \frac{1}{2}\mathcal{T} + \sqrt{\frac{1}{4}\mathcal{T}^2 - \mathcal{D}}, \quad \text{(B2)}$$

where $\mathcal{T}$ and $\mathcal{D}$ denote trace and determinant of $C_{t_0}^t(\mathbf{x}_0)$, respectively, and

$$\xi_1 = \begin{pmatrix} 0 & 1 \\ -1 & 0 \end{pmatrix}\xi_2, \quad \xi_2 = \begin{bmatrix} \dfrac{C_{12}}{\sqrt{(C_{11} - \lambda_2)^2 + C_{12}^2}} \\[4mm] \dfrac{C_{11} - \lambda_2}{\sqrt{(C_{11} - \lambda_2)^2 + C_{12}^2}} \end{bmatrix}, \quad \text{(B3)}$$

where C_{ij} is the ijth entry of $C_{t_0}^t(\mathbf{x}_0)$.

4) Compute the trajectories of the shear vector fields $\chi_\pm(\mathbf{x}_0)$, defined in (5), by solving the differential equation

$$\frac{d\mathbf{x}_0(s)}{ds} = \text{sign}\left\{\chi_\pm[\mathbf{x}_0(s)] \cdot \frac{d\mathbf{x}_0(s - \Delta)}{ds}\right\}\chi_\pm[\mathbf{x}_0(s)], \quad \text{(B4)}$$

with Δ denoting the integration step in s. The factor multiplying $\chi_\pm[\mathbf{x}_0(s)]$ in (B4) removes orientational discontinuities in $\chi_\pm[\mathbf{x}_0(s)]$ arising from the lack of a global orientation for $\xi_i(\mathbf{x}_0)$ (cf. Haller and Beron-Vera 2012, for details).

5) In the phase portrait of $\chi_\pm(\mathbf{x}_0)$, locate all nested families of limit cycles. Such closed shearlines can be located as fixed points of Poincaré maps defined on one-dimensional sections locally transverse to trajectories of (B4). To construct a Poincaré map, one considers a trajectory with initial condition on the section and observes the location at which this trajectory first returns to the section; a fixed point is given by an initial condition that is mapped onto itself (cf., e.g., Ottino 1989, section 5.5).

6) In each nested family of limit cycles, locate a geodesic eddy boundary at time t_0 as the limit cycle with the lowest average geodesic deviation $\langle d_g^{\chi_\pm}(\mathbf{x}_0)\rangle$, with $d_g^{\chi_\pm}(\mathbf{x}_0)$ defined in (6).

7) To track geodesic eddies in time, find their time t positions by applying the flow map $F_{t_0}^t$ to geodesic eddy boundaries identified at time t_0.

APPENDIX C

Numerical Details

All trajectory integrations in this paper were carried using a stepsize-adapting fourth-order Runge–Kutta method. The interpolations involved were obtained from a cubic scheme. Differentiation was executed using finite differences on an auxiliary grid of four points neighboring each point in a regular grid of size 2000^2. Geodesic eddy detection was initialized by searching for regions possibly including closed shearlines. This process was started on a coarser grid of points covering the whole geographical domain of interest. Once a potential geodesic eddy region was identified, a refined calculation in that region was conducted. This involved launching shearlines on a straight segment of 2500 grid points. The Poincaré section was appropriately located across the region to construct a first return map onto this segment for the computation of limit cycles.

REFERENCES

Arnold, V. I., V. V. Kozlov, and A. I. Neishtadt, 2006: *Mathematical Aspects of Classical and Celestial Mechanics. Dynamical Systems III,* Vol. 3, Encyclopedia of Mathematical Sciences, 3rd ed. Springer-Verlag, 517 pp.

Batchelor, G. K., 1964: *An Introduction to Fluid Dynamics*. Cambridge University Press, 660 pp.

Beal, L. M., and Coauthors, 2011: On the role of the agulhas system in ocean circulation and climate. *Nature,* **472,** 429–436.

Beron-Vera, F. J., M. J. Olascoaga, and G. J. Goni, 2008: Oceanic mesoscale eddies as revealed by Lagrangian coherent structures. *Geophys. Res. Lett.,* **35,** L12603, doi:10.1029/2008GL033957.

Biastoch, A., C. W. Böning, J. R. E. Lutjeharms, and F. U. Schwarzkopf, 2009: Increase in Agulhas leakage due to poleward shift of the Southern Hemisphere westerlies. *Nature,* **462,** 495–498.

Chelton, D. B., M. G. Schlax, R. M. Samelson, and R. A. deSzoeke, 2007: Global observations of large oceanic eddies. *Geophys. Res. Lett.,* **34,** L15606, doi:10.1029/2007GL030812.

——, P. Gaube, M. G. Schlax, J. J. Early, and R. M. Samelson, 2011a: The influence of nonlinear mesoscale eddies on near-surface oceanic chlorophyll. *Science,* **334,** 328–332.

——, M. G. Schlax, and R. M. Samelson, 2011b: Global observations of nonlinear mesoscale eddies. *Prog. Oceanogr.,* **91,** 167–216.

Conti, C., D. Rossinelli, and P. Koumoutsakos, 2012: GPU and APU computations of Finite Time Lyapunov Exponent fields. *J. Comput. Phys.,* **231,** 2229–2244.

Doglioli, A. M., B. Blanke, S. Speich, and G. Lapeyre, 2007: Tracking coherent structures in a regional ocean model with wavelet analysis: Application to Cape Basin eddies. *J. Geophys. Res.,* **112,** C05043, doi:10.1029/2006JC003952.

Early, J. J., R. M. Samelson, and D. B. Chelton, 2011: The evolution and propagation of quasigeostrophic ocean eddies. *J. Phys. Oceanogr.,* **41,** 1535–1555.

Fang, F., and R. Morrow, 2003: Evolution, movement and decay of warm-core Leeuwin Current eddies. *Deep-Sea Res. II,* **50,** 2245–2261.

Froyland, G., C. Horenkamp, V. Rossi, N. Santitissadeekorn, and A. S. Gupta, 2012: Three-dimensional characterization and tracking of an Agulhas Ring. *Ocean Modell.,* **52–53,** 69–75.

Fu, L. L., D. B. Chelton, P.-Y. Le Traon, and R. Morrow, 2010: Eddy dynamics from satellite altimetry. *Oceanography (Wash. D.C.),* **23,** 14–25.

Garth, C., F. Gerhardt, X. Tricoche, and H. Hans, 2007: Efficient computation and visualization of coherent structures in fluid flow applications. *IEEE Trans. Visualization Computer Graphics,* **13,** 1464–1471.

Garzoli, S. L., P. L. Richardson, C. M. Duncombe Rae, D. M. Fratantoni, G. J. Goni, and A. J. Roubicek, 1999: Three Agulhas rings observed during the Benguela Current Experiment. *J. Geophys. Res.,* **20** (C9), 20 971–20 986.

Goni, G., and W. Johns, 2001: Census of warm rings and eddies in the North Brazil Current retroflection region from 1992 through 1998 using TOPEX/Poseidon altimeter data. *Geophys. Res. Lett.,* **28,** 1–4.

Gordon, A., 1986: Inter-ocean exchange of thermocline water. *J. Geophys. Res.,* **91** (C4), 5037–5050.

Haller, G., 2001: Distinguished material surfaces and coherent structures in 3D fluid flows. *Physica D,* **149,** 248–277.

——, 2005: An objective definition of a vortex. *J. Fluid Mech.,* **525,** 1–26.

——, and F. J. Beron-Vera, 2012: Geodesic theory of transport barriers in two-dimensional flows. *Physica D,* **241,** 1680–1702.

Henson, S. A., and A. C. Thomas, 2008: A census of oceanic anticyclonic eddies in the Gulf of Alaska. *Deep-Sea Res. I,* **55,** 163–176.

Isern-Fontanet, J., E. García-Ladona, and J. Font, 2003: Identification of marine eddies from altimetric maps. *J. Atmos. Oceanic Technol.,* **20,** 772–778.

Jorba, À., and C. Simó, 1996: On quasi-periodic perturbations of elliptic equilibrium points. *SIAM J. Math. Anal.,* **27,** 1704–1737.

Lehahn, Y., F. d'Ovidio, M. Lévy, Y. Amitai, and E. Heifetz, 2011: Long range transport of a quasi isolated chlorophyll patch by an Agulhas ring. *Geophys. Res. Lett.,* **38,** L16610, doi:10.1029/2011GL048588.

Le Traon, P.-Y., F. Nadal, and N. Ducet, 1998: An improved mapping method of multisatellite altimeter data. *J. Atmos. Oceanic Technol.,* **15,** 522–534.

Lugt, H. J., 1979: The dilemma of defining a vortex. *Recent Developments in Theoretical and Experimental Fluid Mechanics,* U. Muller, K. G. Riesner, and B. Schmidt, Eds., Springer-Verlag, 309–321.

Mézic, I., V. A. F. S. Loire, and P. Hogan, 2010: A new mixing diagnostic and the Gulf of Mexico oil spill. *Science,* **330,** 486.

Morrow, R., F. Birol, and D. Griffin, 2004: Divergent pathways of cyclonic and anti-cyclonic ocean eddies. *Geophys. Res. Lett.,* **31,** L24311, doi:10.1029/2004GL020974.

Okubo, A., 1970: Horizontal dispersion of flotable particles in the vicinity of velocity singularity such as convergences. *Deep-Sea Res. Oceanogr. Abstr.,* **12,** 445–454.

Olson, D., and R. Evans, 1986: Rings of the Agulhas Current. *Deep-Sea Res.,* **33,** 27–42.

Ottino, J., 1989: *The Kinematics of Mixing: Stretching, Chaos and Transport.* Cambridge University Press, 364 pp.

Peacock, T., and J. Dabiri, 2010: Introduction to focus issue: Lagrangian coherent structures. *Chaos,* **20,** 017501, doi:10.1063/1.3278173.

Ridgway, K. R., and J. R. Dunn, 2007: Observational evidence for a Southern Hemisphere oceanic supergyre. *Geophys. Res. Lett.,* **34,** L13612, doi:10.1029/2007GL030392.

Rio, M.-H., and F. Hernandez, 2004: A mean dynamic topography computed over the world ocean from altimetry, in situ measurements, and a geoid model. *J. Geophys. Res.,* **109,** C12032, doi:10.1029/2003JC002226.

Robinson, A. R., Ed., 1983: *Eddies in Marine Science.* Springer-Verlag, 609 pp.

Souza, J. M. A. C., C. de Boyer Montegut, and P. Y. Le Traon, 2011: Comparison between three implementations of automatic identification algorithms for the quantification and characterization of mesoscale eddies in the South Atlantic Ocean. *Ocean Sci. Discuss.,* **8,** 483–531.

Turiel, A., J. Isern-Fontanet, and E. Garcia-Ladona, 2007: Wavelet filtering to extract coherent vortices from altimetric data. *J. Atmos. Oceanic Technol.,* **24,** 2103–2119.

Weiss, J., 1991: The dynamics of enstrophy transfer in two-dimensional hydrodynamics. *Physica D,* **48,** 273–294.